Revealing the sound, flow excitation, and collision dynamics of human handclaps

Yicong Fu [1,2] Akihito Kiyama [2,3] Guoqin Liu [4] Likun Zhang [4] and Sunghwan Jung [2,*]

[1]Sibley School of Mechanical and Aerospace Engineering, Cornell University, Ithaca, New York 14853, USA
[2]Department of Biological and Environmental Engineering, Cornell University, Ithaca, New York 14853, USA
[3]Graduate School of Science and Engineering, Saitama University, Saitama 338-8570, Japan
[4]National Center for Physical Acoustics and Department of Physics and Astronomy, University of Mississippi, University, Mississippi 38677, USA

(Received 13 June 2024; accepted 23 January 2025; published 11 March 2025)

Hand clapping, a ubiquitous human behavior, serves diverse daily-life purposes. Despite prior research, a comprehensive understanding of its physical mechanisms remains elusive. To bridge this gap, we integrate *in vivo* human data, parametric experiments, finite-element simulations, and theoretical frameworks to investigate the acoustic properties of clapping sound and their connections with the fluid flow and soft matter collision. Motion-audio synchronization reveals the flow-excitation nature of the hand cavity resonance. The classical Helmholtz resonator model, incorporating occasional pipe standing wave contributions for finger grooves, reliably predicts clapping sound frequencies across various real and engineered hand configurations. Material elasticity, coupled with the dynamic collision process, has minor effects on the sound frequency but a major impact on the temporal evolution of the sound signals, as reflected by the quality factors of resonance. Both spatial and dynamic factors for sound intensity are examined. We establish a quadratic scaling relationship between hand cavity gauge pressure and clapping speed, elucidating the positive correlation between faster claps and louder sounds. Our work advances the knowledge of hand-clapping acoustics and offers insights into sound signal synthesis, processing, and recognition. Furthermore, these findings may facilitate low-cost acoustical diagnostics in architecture and enhance rhythmic sound patterns in music and language education.

DOI: 10.1103/PhysRevResearch.7.013259

I. INTRODUCTION

Human hand clapping is a common rhythmic behavior that involves impacting the hands together. It serves as a vital form of nonverbal communication that is complex and situational. When performed by large audiences, clapping expresses appreciation and joy, often resulting in collective acoustic synchronization [1]. Hand claps are extensively used in music to aid in identifying rhythms [2,3]. This usage has a significant impact on children's playground music education [4] and traditional African drum beats [5]. Clapping is also employed in foreign language education to help memorize specific words and pronunciations [6,7]. Hand claps are also of great value for engineering for their potential as an impulsive, easily acquired sound source for architectural acoustic performance analysis [8–10]. The energy generated by hand clapping can be harnessed for a self-contained, wearable, and sustainable power supply [11]. Recent studies also linked clapping to brain activities, suggesting possible biomedical implications [12]. Furthermore, computer vision and machine learning can be used to analyze clapping motion and sound, providing a basis for individual identification [13,14] and action recognition [15]. There has also been an increasing emergence of biomechanical and fluid mechanical investigation on human upper-limb sound-generating motions such as clapping of wet hands [16] and finger snapping [17], which motivate our present work.

Despite the simplicity of manipulating upper limb motion to create different clapping sounds, this sound generation is a complex and unsteady process involving soft-body collision and acoustic wave propagation. There had been only a few attempts to understand the acoustic property of handclapping sounds. Repp's pioneering work on spectrum analysis initially proposed the potential of human identification [18]. Repp analyzed eight different hand configurations from 20 participants and demonstrated the relevance between hand configuration and frequency responses. His work suggested the existence of the individual clap signature, while the theoretical framework was yet unclear. Later, Fletcher [19] attempted to explain the complex physics with three extremely simplified geometry modes. (1) In the case of convex-convex surface impact, little sound is produced. (2) If two surfaces are complementary, then a high-frequency but nonresonating sound results from the shock wave, which was also experimentally observed in previous research [20]. (3) In the case of concave-concave surface impact, enclosing an air cavity, a sound with central resonance frequency occurs, which Fletcher proposed to be modeled by the well-known Helmholtz resonator (HR) [21].

Flow-induced sounds have recently received broad attention [22–25], within which Helmholtz resonator has been

*Contact author: sj737@cornell.edu

one of the fundamental paradigms for both aerial and water acoustic analysis. Helmholtz resonators were initially created by Hermann von Helmholtz as a volume-resonating device. A simple example is to create tunes by blowing air across the opening of an empty bottle, whose effect is studied in similar flow-excitation settings [26,27]. The physics of HR has been largely studied in the aspect of geometries [28–30] and patterns [31,32]. Historically, the concept has been used widely in musical instrument designing such as ceramic whistles and ocarinas [33]. Large-scale effects have also been explored in architecture for sound absorption purposes [34]. In recent years, scholars also borrowed the HR theory to model the sound creation by insects [35].

Human hand claps, to the best of our knowledge, have not received substantial work to cross-confirm the HR theory and the experimental observations by parametric studies. In the present work, we employed both reduced-order models and human subjects to evaluate the acoustic performance of clapping sounds in various hand configurations. Acoustic recordings coupled with high-speed images and pressure sensing allowed us to identify and synchronize four dynamic processes important to handclapping acoustics, including fluid motion, sound, pressurization, and soft material deformation. We not only revealed the contributors to the frequency response and the initial sound intensity but also determined the factors affecting damping and propagation. Our spectral analysis validated the relevance of hand configurations to their corresponding sound frequencies through successful modeling by the classical HR and the situational standing wave in finger grooves (viewed as cylindrical pipes). Meanwhile, the limitations of such an HR model due to the assumptions of rigid boundary, static excitation, and negligible energy losses in modeling handclaps' spatiotemporal evolution were discussed. We demonstrated that the transient processes due to various collision speeds and material softness are indeed major factors for the special characteristics of clapping sound.

II. MATERIALS AND METHODS

A. Sample preparation

1. Human subject

Ten participants between the ages of 18 and 70 were recruited to clap in cupped, palm-palm, and palm-finger hand configurations [Fig. 1(a)]. Each person stood at the same relative position from the microphone and clapped consecutively 20 and 30 times under each hand configuration. After every clapping series, the three-dimensional (3D) topology of the receiving hand was scanned for 250 frames from a global angle while maintaining the shape (Polycam, iPhone app). Geometries were reconstructed into 3D point clouds (Supplemental Material Sec. II A [37]), from which important dimensions were extracted using MathWorks™ MATLAB 2023b (shortened as MATLAB hereafter). Length measurement uncertainties were approximately 5%.

2. Hand replicas

In order to conduct controlled parametric studies, soft polymer hand replicas were fabricated to generate clapping sounds. To resemble the human skin elasticity to the same order of magnitude [38–41], Smooth-On Ecoflex™ 0030 silicone (shortened as Ecoflex 0030 hereafter) was chosen. Casting moulds were designed in SolidWorks 2022 and 3D printed in PLA by an Ultimaker S5 FDM printer. Ecoflex 0030 A and B parts were homogenized at a 1:1 volumetric ratio before casting. No degassing was done to liquid silicone since air bubble entrainment was minimal and thought to have a negligible effect on the postcure material property. Each replica was left to cure for at least 4 h before testing to ensure the same stabilized shore hardness. To vary material elasticity, the same fabrication process was used for the softer version made of Ecoflex Gel and two stiffer versions made of Zhermack Elite Double A8 and A16. The minimum cure time was 4 h, 20 min, and 10 min, respectively, according to the companies' manuals. Characterization of the material properties under relatively slow and fast loading conditions can be found in Appendix A.

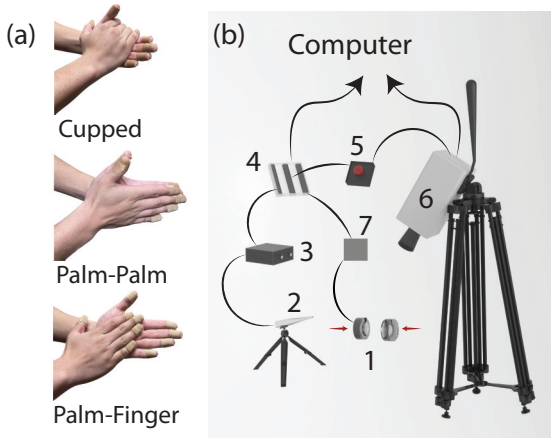

FIG. 1. Illustration of the major experimental materials and methods used in the present work. (a) Three representative hand configurations, also well documented in previous works involving human subjects [14,18,36]. (b) Full synchronous measurements near the sound source. 1: Handclap; 2: Microphone; 3: Signal amplifier; 4: NI DAQ; 5: Trigger; 6: High-speed camera; 7: Pressure sensor.

B. Measurements near the sound source

A full experimental setup for synchronized measurements of the sound, cavity pressure, airflow, and material deformation involves the equipment illustrated in Fig. 1(b). Real human or soft replica handclaps were administered in a room where temperature, humidity, and ambient pressure were relatively controlled. Sound signals were captured by an omnidirectional condenser microphone (EarthWorks Audio QTC40) positioned at 0.05–0.1 m (replica) or 0.15–0.2 m (human) from the sound source. Microphone signals sequentially passed through a preamplifier (PreSonus AudioBox USB 96; gain set to 0 dB), a National Instruments Corp. NI-USB-6216 DAQ card (shortened as NI DAQ hereafter), and a MATLAB Analog Input Recorder (Data Acquisition Toolbox™) at a sampling rate of 96 or 100 kHz. High-speed cameras (Photron Fastcam NOVA S6) were positioned above and aside from the clapping hands to record the material deformations indicated by black tracer dots (Supplemental Movie S3 [37]) and the

impulsive airflow (Sec. III B), respectively. Camera shutters were controlled by a mechanical trigger, whose signal was also passed into the NI DAQ for synchronization. Meanwhile, a differential pressure sensor (MPX 5050GP) was connected to a flexible thin tube (0.72 m) with the other end fused to a syringe needle. The needle was punctured into the replica such that the opening of the needle stayed roughly at the geometric center of the cavity. Pressure signals were passed into the NI DAQ and recorded synchronously. The sensor measured the difference between the cavity pressure and the ambient atmospheric pressure such that the readings represented the change of air pressure within the cavity, i.e., cavity gauge pressure (P_{cavity}). During isolated investigations on every aspect of the handclap where a full synchronization was unnecessary, only relevant equipment would be used and the rest were disengaged from the experimental setup.

C. Simulations near the sound source

Numerical results were obtained for the same geometries as the hand replicas. Simulations were performed in the commercial software COMSOL Multiphysics, specifically employing the pressure acoustics module to model sound resonance within the chamber. The governing equation for acoustic wave propagation is represented as

$$\nabla \cdot \left(-\frac{1}{\rho}(\nabla P - \mathbf{q}_{\text{d}})\right) - \frac{\omega^2 P}{\rho c^2} = Q_m, \tag{1}$$

where ρ denotes the density of air, c denotes the speed of sound in air, ω denotes the angular frequency of acoustic oscillation, and P denotes the instantaneous sound pressure. The terms $\mathbf{q}_{\text{d}}$ and Q_m correspond to the optional dipole and monopole sources, respectively. In our configuration, except on the boundary at the neck outlet (Fig. 2, blue surface), there is no source ($Q_m = 0$) or polarization ($\mathbf{q}_{\text{d}} = 0$) for the longitudinal sound waves. At the neck outlet, a harmonically oscillating pressure $P_0(t) = P_0 e^{i\omega t}$ with an input pressure of 1 Pa is applied, driving the resonance within the chamber.

Inside the chamber, the mesh was constructed using free tetrahedrons, as shown in Fig. 2 (zoomed-in image). The maximum element size, δ_{max}, was set to 1/10th of the minimum wavelength λ_{min} of the acoustic field for the designated scanning frequency range. The scanning frequency range was between 0.1 and 5500 Hz, with c approximated at 340 m/s. The corresponding minimum wavelength is $\lambda_{\text{min}} = \frac{340\,\text{m/s}}{5500\,\text{Hz}} = 0.0618$ m. The maximum element size is $\delta_{\text{max}} = 0.1\lambda_{\text{min}} = 6.18$ mm. Varying the mesh size yielded consistent results that confirmed a robust convergence, verifying that our selection of mesh size was appropriate (Appendix B).

Outside the chamber was also simulated to elucidate the emission of the acoustic waves into the external space. As depicted in Fig. 2, right image, a sphere with a radius of 1 m, filled with air, was modeled to represent an unbounded external environment devoid of reflective surfaces at the domain's outer boundary. Adjacent to this air-filled sphere, a perfectly matched layer (PML) of 0.1 m in thickness was implemented to absorb all outgoing sound waves, thereby mimicking an open space. The mesh for the simulation was designed using free tetrahedral elements, with the maximum element size restricted to one-fifth of the acoustic wavelength, ensuring a detailed and accurate representation of the sound field.

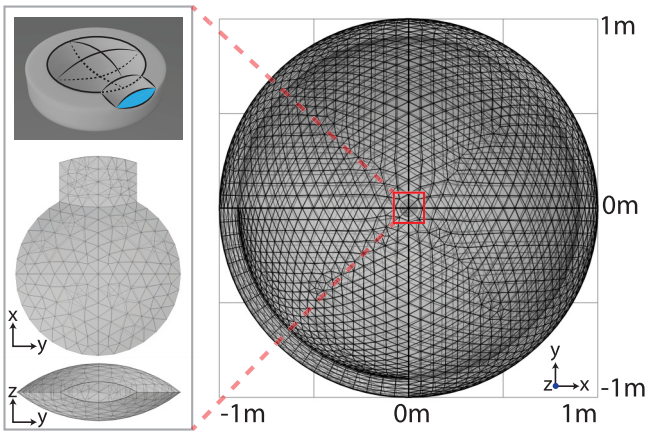

FIG. 2. Mesh setup in COMSOL Multiphysics for simulations near the sound source. The zoomed-in region shows the acoustic chamber inside the clapping hand replicas. Specifically, the top drawing shows the outline of the acoustic chamber enclosed by the replica pair (upper piece omitted). The blue surface indicates the neck outlet to which an oscillating pressure input is applied. The lower two images show the mesh grid of this acoustic chamber from two orthogonal angles. This acoustic chamber with its surrounding solid structure is situated at the center of the 1-m-radius spherical mesh space (right image) which simulates an unbounded external environment.

III. RESULTS

A. Helmholtz resonator

The geometry of clapping hands and the resulting fluid patterns showed the resemblance between human hands and Helmholtz resonators (Supplemental Movies S1 and S2 [37]). The traditional HR chamber consists of a substantial cavity and a narrow outlet via a neck. It was reasonably intuitive to consider the air pocket enclosed between the palms as the equivalent to the cavity volume of HR, V. However, defining the neck and the outlet proved less straightforward, requiring direct visualization of the fluid motion and pressure field distribution.

To visualize the fluid motion on collision, we introduced dry baby powder (Johnson & Johnson Co.) into the palm cavity. Across all three configurations, a consistent outcome was observed: the expulsion of an air jet through the purlicue (the opening between the thumb and the index finger) (Supplemental Movie S1 [37]). Thus, we defined the purlicue opening area as the outlet area S, the direction of the jet as the neck orientation, and the rim extending beyond the palm cavity along the path of the jet as the neck length L. Empirically, an end correction is normally applied on L to account for the radiative effect of acoustic oscillations, giving the effective neck length L' [21].

Reduced-order elastic replicas that captured the fundamental geometric parameters, cavity volume (V), outlet area (S), and effective neck length (L'), were created based on the measurable dimensions shown in Fig. 3(a). Definitions for V,

TABLE I. Nominal design values for hand replicas in comparison with their realistic reference ranges from human participants (raw data in Supplemental Material Sec. II B [37]).

Type	V (mm^3)	S (mm^2)	L' (mm)
Human	$44,400 \pm 41,300$	187 ± 103	26.32 ± 5.46
V1	11 800		26.09
V2	24 000		23.24
V3	36 800	80.2	21.79
V4	50 500		21.66
V5	65 400		21.14
S1		65.4	21.30
S2		92.4	22.72
S3	36 800	117.7	24.06
S4		163.1	26.35
S5		281.5	31.57
L1			16.02
L2			22.22
L3	36 800	163.1	26.35
L4			31.80
L5			35.99

S, and L' are as follows:

$$V = \tfrac{1}{3}\pi H(3R^2 + H^2), \tag{2}$$

$$S = \tfrac{1}{2}R_{\text{curv}}^2[\theta - \sin(\theta)], \tag{3}$$

$$L' = L + 1.2\sqrt{S/\pi} = \tfrac{1}{2}(L_{\text{mid}} + L_{\text{side}}) + 1.2\sqrt{S/\pi}, \tag{4}$$

where $R_{\text{curv}} = (h^2 + 0.25w^2)/2h$ and $\theta = \arcsin(w/2R_{\text{curv}})$. Then they were each varied by five levels (V1–V5; S1–S5; L1–L5) to encapsulate a wider range of shapes mimicking the different hand configurations in reality, as shown in Table I. Air jets around the replicas were similar to the real human handclaps, indicating a consistent pattern of fluid flow (Supplemental Movie S2 [37]). Further, the replicas were simulated with the same geometries and material properties under static (noncollision) excitation. The sound pressure amplitude on the two-piece-contacting plane inside the replica chamber changes rapidly along the neck while staying relatively constant in the cavity, consistent with that of a traditionally shaped HR with a large spherical cavity and a narrow cylindrical neck [Fig. 3(b)]. Both experimental and simulation results validated the application of the HR model in simplifying and understanding the human handclap acoustics.

B. Dynamic processes

The handclapping phenomenon is highly dynamic, involving transient behaviors of the airflow, acoustic signal, cavity pressure, and soft material deformation. Synchronized quantification of all four timescales assisted us in determining the HR resonance as the dominant sound generation mechanism and physically separating the contributing factors to different aspects of the sound. The aforementioned baby powder airflow visualization technique was used on three pairs of hand replicas, $V1$, $V3$, and $V5$. The same jet flow was visible during the sound generation [Figs. 4(a1)–4(c1) and 4(d)]. No

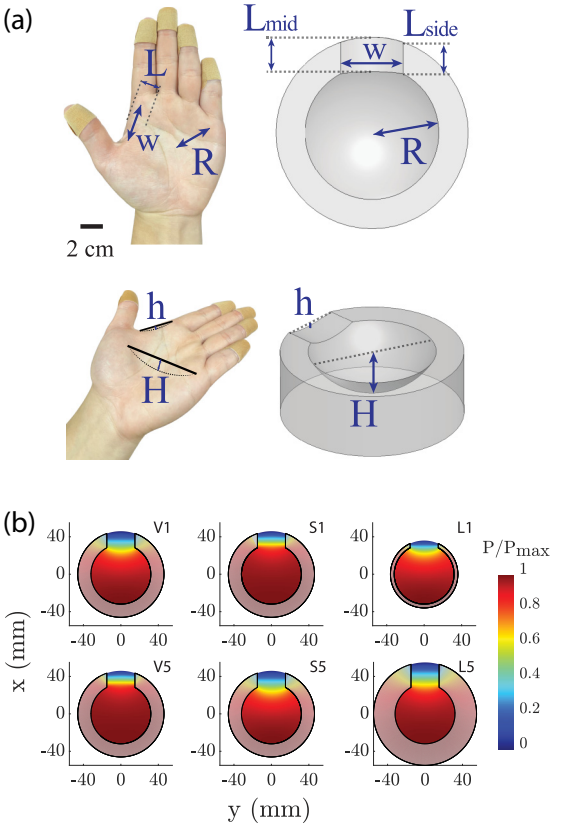

FIG. 3. Reduced-order modeling of human hands to the Helmholtz resonator. (a) Dimensional comparison between real hands and replicas showing the measurable lengths and scales used to calculate V, S, and L'. The scale bar represents the human hand images. (b) Simulated sound pressure max amplitude field on the central impacting plane inside the replicas showing resemblance with traditional HRs.

jet was observed when two hand pieces were still approaching each other or during the initial stage of the solid material impact ($t < 0$ ms). At $t = 0$ ms, the first and strongest jet emerged from the neck opening. For $t > 0$ ms, the first jet moved farther and dissipated, while secondary and/or tertiary jets emerged [Figs. 4(a2)–4(c2)]. The sound dynamics [Figs. 4(a3)–4(c3) top curves] proved to be consistent with the airflow dynamics. No sound was identifiable when two pieces were approaching each other before the collision. Minimal sound disturbances were visible immediately following the collision ($-10 < t < 0$ ms), proving that solid material vibration is not the major contribution to handclapping sounds. Simultaneous with the initial emergence of the jet ($t = 0$ ms), the clapping sound reaches the first peak of its large-amplitude oscillation, proving that the airflow is key to handclapping sound generation. Then the clapping sound decays in the next approximately 10 ms. Cavity gauge pressure further presented evidence for the jet flow. The momentum of colliding hands led to structural deformations that compressed the cavity momentarily to create an elevated internal pressure. As P_{cavity} reached a maximum, the neck outlet was forced open to release air in a jet flow. Thus, the initial peak P_{cavity} occurred just before the emergence of the jet flow, corresponding to the initial peak of the sound at $t = 0$ ms [Figs. 4(a3)–4(c3)

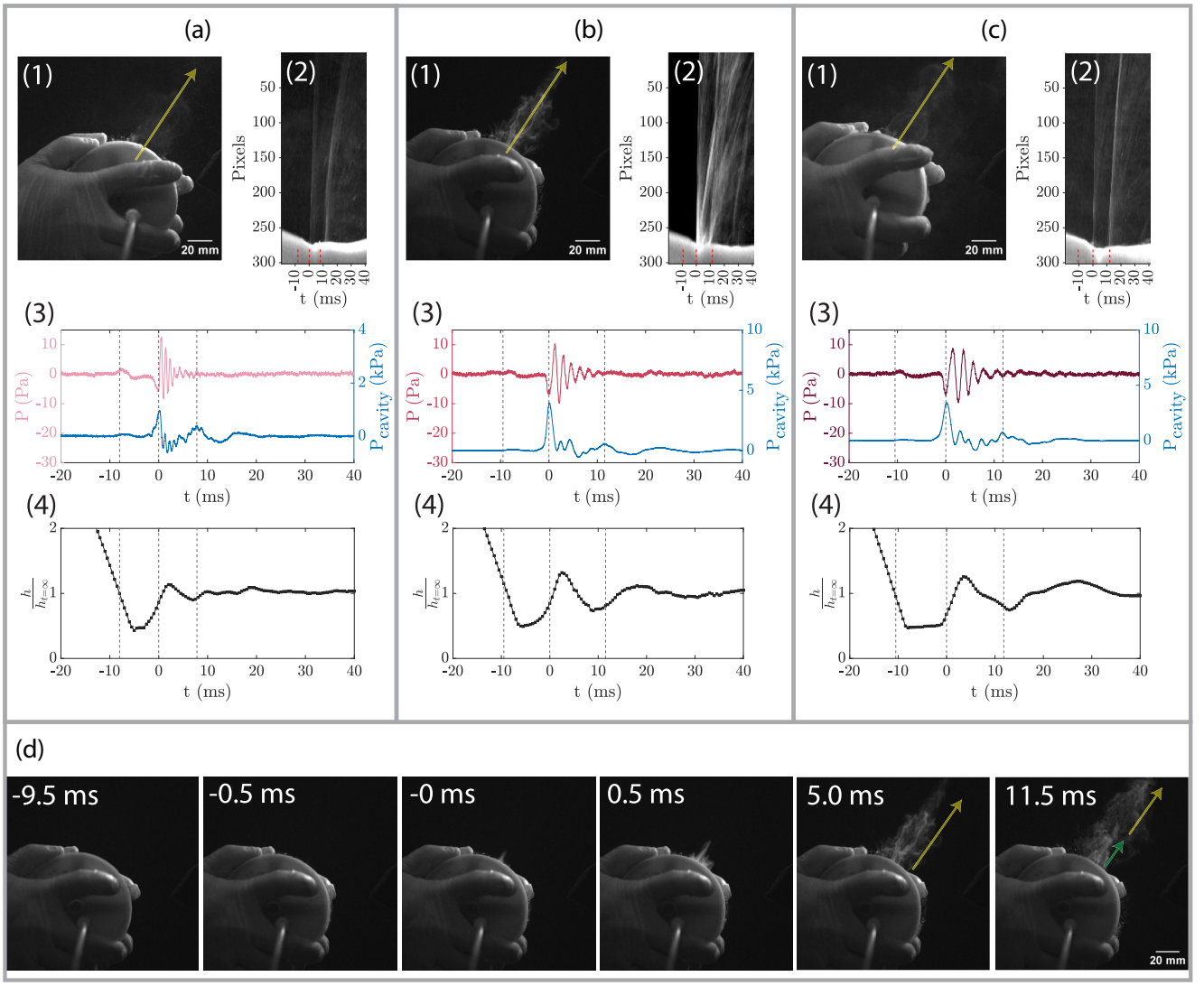

FIG. 4. Synchronized timescales for dynamic processes during Ecoflex 0030 hand replica collisions. (a), (b), and (c) represent three different geometric configurations $V1$, $V3$, and $V5$, respectively. (1) Air jet flow at 5 ms after the initial peak of the clapping sound signal. (2) Time-sequential compilation of the pixel color intensities along the central direction of the jet flow, indicated by the arrow in (1). The light-colored substrate is the silicone rim. The near-vertical light-colored streaks are the front of the jet flow, seeded with baby powder. Red dashes mark three crucial time instants: initial solid material collision (left), initial sound signal peak (mid), and secondary cavity gauge pressure peak (right). (3) Overlaid sound pressure (P) and cavity gauge pressure (P_{cavity}). $t = 0$ ms is defined as the initial peak of the sound pressure signal, consistent with (2). The cavity gauge pressure curve is generally shifted forward in time by 2.1 ms to account for sound wave propagation within the tubing of the pressure sensor (a 72 cm travel at 340 m/s). Dashed lines mark the same time instants as in (2). (4) Dynamic outlet deformation in terms of arch height (h). The same dash lines were used. (d) Time series of the airflow in (b). $t = -9.5$–0.5 ms is during solid material collision and cavity pressurization, and no jet flow is created. $t = 0$–5 ms shows the emergence of the primary jet flow, leading to the clapping sound. $t = 11.5$ ms shows the emergence of a secondary jet flow due to the postcollision deformations. The yellow arrow indicates the first jet and the green arrow indicates the second jet.

bottom curves]. Close examination of the P_{cavity} could identify the superposition of a low-frequency large-amplitude waveform due to the cavity geometry oscillation after the collision and a high-frequency small-amplitude waveform attributed to the sound. The trailing cavity geometry oscillation ($t = 10$–30 ms) explained the emergence of the secondary and/or tertiary jets but did not result in additional clapping sound generations.

The jet flow may have two possible effects on the sound generation: providing the initial excitation to the HR and turbulent noise. To decouple and evaluate, we quantified the jet velocity (u_{jet}) at the outlet. Given the sudden pressurization and the strong jet, isentropic relations can be employed to predict u_{jet}. Assuming ideal gas for air and P_{cavity} driving the flow through a narrow duct, the Mach number at the neck outlet is

$$M = \sqrt{\frac{2}{\gamma - 1}\left[\left(\frac{P_{\text{cavity}} + P_{\text{atm}}}{P_{\text{atm}}}\right)^{\frac{\gamma-1}{\gamma}} - 1\right]}, \tag{5}$$

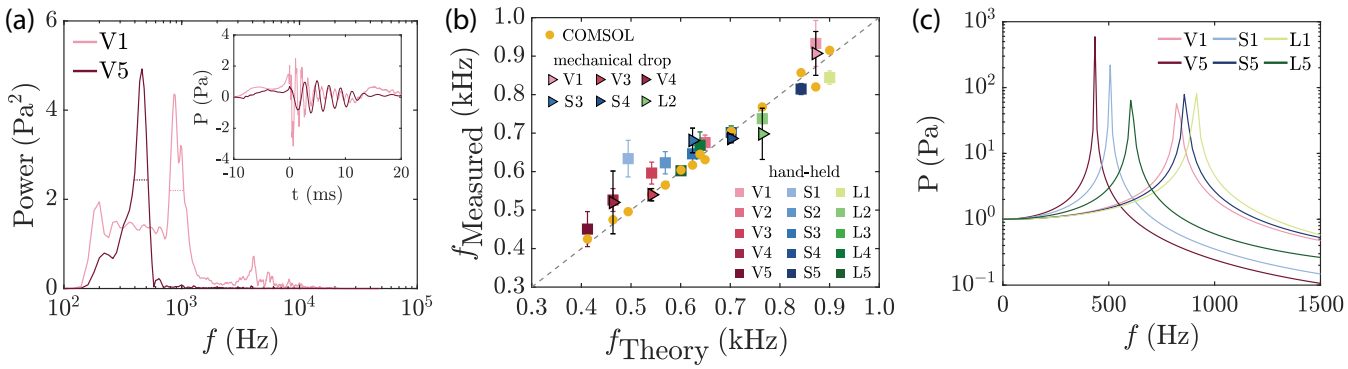

FIG. 5. Replica handclapping sound frequency changes with the configurations. (a) FFT spectrogram and the respective raw signal oscillograms (inset) of two silicone replicas with highly different cavity volumes ($V1$ and $V5$). Note: Dashed line segments on the FFT spectrogram represent the 50% power level from which mean frequency and quality factors are computed. (b) Comparison between the measured frequencies from silicone replicas in both experiments and simulations against the theoretical predictions by the proposed HR theory. Note: Six examples from the mechanical drop test (Appendix D) were included as a comparison with the hand-held test data to confirm the repeatability and consistency of both testing methods. Error bars represent standard deviations. (c) Resonance frequency peaks of the different silicone replica geometries under static excitation yielded by simulations (full results refer to Supplemental Material Sec. III A [37]).

where $\gamma = 1.4$ is the specific heat ratio of air and $P_{\text{atm}} = 101.3$ kPa is the ambient atmospheric pressure. For a typical P_{atm} of 0.1–5 kPa for handclaps [see Figs. 4(a3)–4(c3) and Fig. 8(c)], the Mach number falls in the range of 0.04–0.26, equivalent to a u_{jet} of 13–90 m/s if the speed of sound (c) is taken as 340 m/s. The experimental value of u_{jet} can also be roughly estimated by manually tracking the front of the jet powder, which proved to be consistent with the model prediction. The Reynolds number of the jet flow can be defined as $\text{Re} = \rho u_{\text{jet}} D/\mu$, where $\rho = 1.23\,\text{kg/m}^3$ is the air density, $D = 2\sqrt{S/\pi}$ is the characteristic length scale of the neck opening, and $\mu = 1.8 \times 10^{-5}$ Pa s is the air dynamic viscosity at 20 °C. This resulted in a Re within 8000–103 000, indicating that the jet was turbulent. Generally, the turbulent-jet-induced sound would behave similarly to a broad-band noise, absent of a dominant oscillation frequency which is characteristic to the handclapping sound. The motion of the powder shows that this turbulent jet persists much longer than the clapping sound signal. The range of u_{jet} also predicts the turbulent noise at negligible intensity compared with the clapping sound. Therefore, we conclude that the human handclapping sound is generated neither by the solid material vibration postcollision nor by the jet turbulence but by the Helmholtz resonance excited by the initial emergence of the jet at the neck of the hand-enclosed chamber. The first jet functions as the initial perturbation to the spring-mass system within the HR (Appendix C). Subsequently, the air column within the neck oscillates at the natural frequency after the initial perturbation until the energy dissipates due to damping losses.

While the outlet deformation dynamics [Figs. 4(a4)–4(c4)] does not affect the initial handclapping sound generation, it has a major influence on the temporal dissipation of the sound. During the major sound emission period ($t = 0$–10 ms), the outlet size exhibits a significant change, introducing extra losses and nonlinear effects to the HR resonance. The vibration of the soft material incurs more viscoelastic, viscous boundary layer, and structural damping to the acoustic signal, resulting in a faster decay and a broader frequency bandwidth, which will be discussed in detail in Sec. III E.

C. Sound frequency

1. Frequency dependence on configuration

Changing the hand shapes to alter the pitch of the clapping sound is intuitive as people usually use and recognize the cupped configuration for a deeper sound and the palm-finger configuration for a higher sound. This can be both qualitatively and quantitatively demonstrated with our silicone replicas, as shown in Fig. 5(a). V1 and V5, with very different cavity volumes (see Table I), produced distinctive resonance peaks in the fast Fourier transformation (FFT) spectral analysis, indicating that the sound signals had different dominant frequency compositions as expected. The pitch difference was not only audible but also visible on the oscillogram [see the inset of Fig. 5(a)] as they had obviously different oscillation periods.

The theoretical framework for a traditional HR under static excitation has been thoroughly established [21]. The frequency response of such an HR is a function of the speed of sound and three geometric parameters, expressed as

$$f = \frac{c}{2\pi}\sqrt{\frac{S}{VL'}}. \tag{6}$$

Several assumptions are necessary to adopt this theory in our problem: (1) the timescale of the acoustic sound is significantly shorter than the material relaxation timescale and thus the clapping hands can be approximated as a static snapshot of the classical HR at an instantaneous moment, (2) sound leakage through the solid structures is minimal, and (3) all silicone replicas have cavities large enough compared to the volume of the neck, in contrast with other resonating chambers.

Experimental results from the silicone replicas demonstrated excellent agreement with the theoretical frequency predictions [Fig. 5(b)]. Specifically, larger cavity volumes and longer neck lengths produced lower sound frequencies, while larger outlet areas resulted in higher sound frequencies. However, we observed a slight deviation in the trend for smaller outlet areas (S1 and S2). This is likely due to the

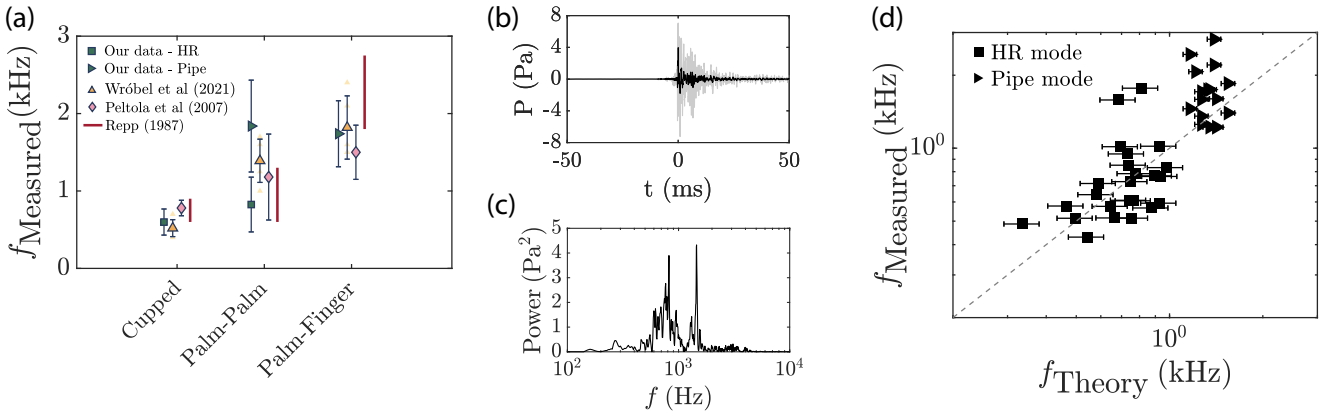

FIG. 6. Human handclapping sound frequency dependence on the configurations and comparison with acoustic models. (a) Present work's human handclapping sound frequency comparison with previous literature. (b) Signal averaging of sequential claps under the same configuration from the same individual (separate claps in gray; mean signal signature in black). (c) FFT of the aforementioned mean signal, showing both the HR mode and the pipe mode. (d) Comparison between the measured frequencies from human participants against the theoretical predictions. Horizontal error bars represent 13% and 5% errors for the HR and the pipe modes, respectively, attributed to uncertainties in the length measurement.

overexpansion of the outlet, where the pressurized air jet squeezed out of the cavity forcefully and pushed the soft material outward, effectively making the outlet bigger than the design value and thus exceeding the prediction (Supplemental Material Sec. I C [37]). Simulations also recorded the first (lowest) resonance peaks yielded by frequency scans of every replica geometry [Fig. 5(c)], showing good agreement with both the HR theory and the experiments [Fig. 5(b)].

A similar analysis was carried out for real human hand claps. Assuming a symmetric shape for the striking hand in cupped and palm-palm, and a flat plate in palm-finger, dimensions in Table I were used to predict the theoretical frequencies using Eq. (6). We first compared our results with those reported in other research [14,18,36]. A similar trend of increasing frequency as the configuration changed from cupped to palm-palm and then to palm-finger was consistent with others, as well as the frequency magnitudes [Fig. 6(a)]. To improve the signal repeatability, claps of the same hand configuration from the same individual were phase-averaged to extract the mean signal signature (Supplemental Material Sec. II C [37]), as shown in Fig. 6(b). Some individuals yielded two distinctive frequency peaks: one lower, broader-band peak and one higher, narrower-band peak [example in Fig. 6(c)]. We interpret that the lower peak (<1000 Hz) is associated with the HR resonance, while the higher peak (>1000 Hz) is associated with sound emission from the finger grooves when fingers come in contact with the receiving hand. The finger grooves, which are closed at one end and open at the other end can be considered as a single-open-ended pipe to emit sound whose lowest-mode frequency is predicated as $f = c/(4L_{\text{pipe}})$ without end corrections [21]. Measurements from human participants' fingers indicate L_{pipe} falls in the range of 6.44 ± 0.55 cm [Fig. 7(a)], yielding a frequency around 1320 ± 113 Hz, consistent with the higher peak in Fig. 6(c). As a result, separating the HR mode and the pipe mode for human hand claps showed decent agreement between the measurements and the theory [Fig. 6(d)]. One may notice that the pipe mode sound from finger grooves exhibits a wider vertical dispersion in the experiments than in the theoretical model [Fig. 6(d)]. We believe this is attributed to personal clapping preferences and discrepancies in measurable hand dimensions. The theoretical predictions were based on the lengths of undeformed fingers that presented virtually no deformation. They represent the lower limit of pipe mode frequency contributions from each individual. Their dispersion is mostly due to the size variation of natural human hands. Conversely, experimental values have more uncertainties. Human subjects were not explicitly specified to use the full length of their fingers to strike the receiving hand, thus the effective L_{pipe} involved in sound generations may be smaller than expected if only a portion of the fingers participated in the collision, per personal preferences. The collision also deforms the hand tissue, which may result in shorter instantaneous finger grooves for sound generation. Both factors can reduce the experimental L_{pipe}, resulting in a higher value than the theoretical prediction, explaining the upward trend. The same hand-size variation remains in experiments, while two new sources of uncertainties were added, leading to a wider dispersion. Idealized and controlled experiments using Ecoflex 0030 finger groove replicas further validated the contribution of the pipe mode in handclapping sound. Two silicone pieces with half-circular cylindrical grooves of different lengths [Fig. 7(b)] were clapped onto a flat silicone surface [Fig. 7(e)] in comparison with striking extended human fingers to palm [Fig. 7(c)] or the same flat silicone surface [Fig. 7(d)]. Only the pipe mode was preserved in these sound-generating collisions while the HR mode was completely eradicated. FFT showed excellent agreement between the experimental frequency and the pipe mode theory, verifying the sound contribution from finger grooves [Fig. 7(f)].

2. *Frequency dependence on elasticity*

The structural deformation in the hand HR geometry resulting from the soft-body collision may potentially deviate the frequency from theoretical predictions based on nondeformable bodies. Two major contributors are the clapping speed (u_{clap}; measurement method see Supplemental Material Sec. I A [37]) and the material elastic modulus (E).

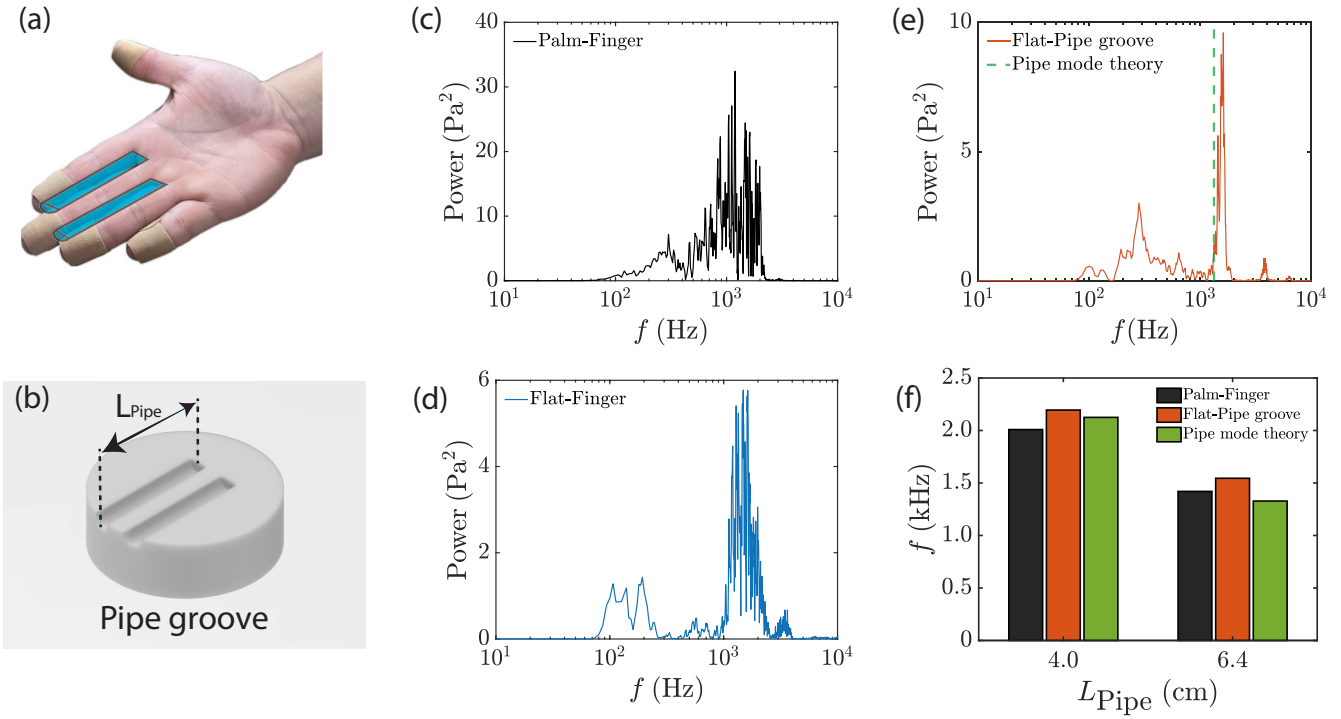

FIG. 7. Human and replica validation of the finger grooves' contribution. (a) Finger grooves on human hands. (b) Semi-circular cylindrical groove replica made of Ecoflex 0030. [(c)–(e)] The sound frequency composition of three finger-clapping conditions. (f). Finger groove sound frequency changes with groove length, as predicted by the pipe mode theory.

Actively controlling the collision speed of the silicone replicas showed that overall, u_{clap} has limited impact on the resulting sound frequency (Supplemental Material Sec. I B [37]). When two hands collide, there would be a certain amount of deformation causing a finite change $d\xi$ in the fundamental geometric parameters ($\xi \equiv V$, S, or L). $|d\xi|$ increases for higher u_{clap}, resulting in a higher ratio of $|d\xi/\xi|$, theoretically leading to more influence on the frequency. However, this ratio is also affected by the denominator ξ, i.e., the nominal design value of the fundamental geometries. Therefore, at a certain u_{clap}, a smaller nominal value from configurations such as V1, V2, S1, and S2 would make the corresponding $|dV/V|$ and $|dS/S|$ larger to cause a more pronounced frequency drift, explaining the positive correlations. However, due to the material properties of Ecoflex 0030, the deformation attributed to varied collision speed is not significant enough to cause a notable sound frequency shift.

To investigate the effect of material elastic modulus, soft polymers with different postcure shore hardness were used while maintaining a constant geometry. Experimental results showed a slightly increasing frequency with stiffer materials (Supplemental Material Sec. I D [37]). Visualizations of the deformation during sound production revealed that the slow and insufficient material retraction around the outlet of the softer models forced the outlet area S to be smaller than the nominal design value, resulting in a lower frequency. However, we acknowledge that the lower frequency observed in the softer material could be a combined result of both material deformation and the physics inherent to elastic-wall HR [42–44].

D. Initial sound intensity

To characterize the loudness perception of clapping sounds, we examine the sound pressure field very close to the clapping source. The initial sound intensity is crucial for handclaps to serve the communication purpose and is thought to directly correlate to the HR-exciting jet.

Intuitively, a faster clap would generate a louder sound, as proved by the strong positive correlation in Fig. 8(b). Synchronized measurements of P and P_{cavity} confirmed that the initial peak of the sound signal corresponds to the initial cavity pressurization and the jet expulsion at $t = 0$ ms [Figs. 4(a)–4(c)]. A physical model involving kinematics and material deformation dynamics helps relate the collision speed u_{clap} with the resultant P_{cavity}. Assuming nontrivial deformation due to the collision only occurring in the normal direction to the impacting plane (i.e., along the u_{clap}), we can take a general derivative of Eq. (2) to express the change in cavity volume δV as

$$\delta V = \pi(R^2 + H^2)\delta H, \tag{7}$$

where δH is the cavity height deformation [R and H definitions in Fig. 8(a)]. Then assuming the viscoelastic material behaves like a linear-elastic (Hookean) material under such rapid loading (Appendix A), we can write the material strain as

$$\epsilon = \frac{\delta N + \delta H}{N + H} = \frac{F}{AE}, \tag{8}$$

where F is the impact force, A is the contact area of the two colliding replicas, and E is the elastic modulus. Applying

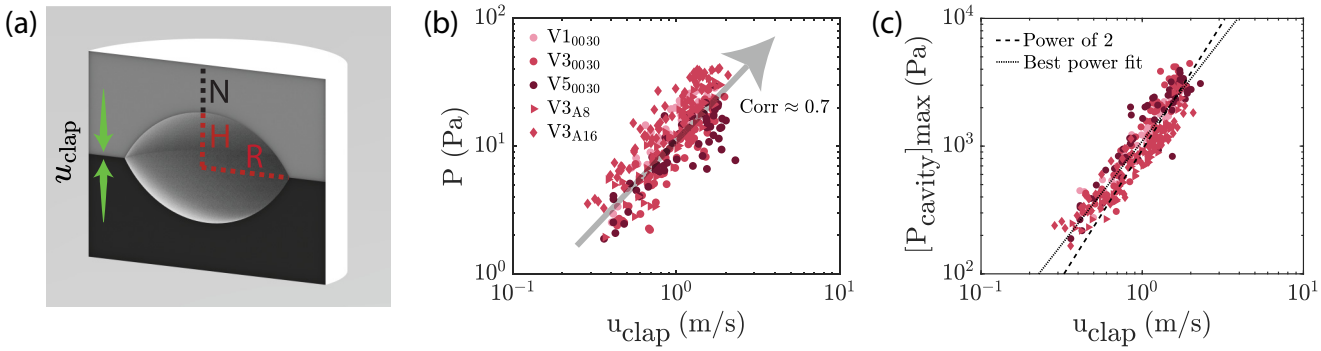

FIG. 8. Initial sound intensity reflected by sound pressure and cavity gauge pressure. (a) Sagittal section of two colliding replicas. The HR cavity has a half-height of H and a radius of R. The material thickness above the apex of the cavity is N and is kept at 6 cm for all replicas, mimicking the thickness of the human hand palm center soft tissue. Two pieces collide at a relative speed of u_{clap}, causing cavity deformation which leads to the pressurization within the cavity P_{cavity}. (b) Positive correlation between the sound pressure and the clapping speed regardless of the configuration or material. i.e., faster claps create louder initial sound intensity. Subscripts in the legend indicate the shore hardness reported by the manufacturers. Detailed measurements of their elastic moduli (E) can be found in Appendix A. (c) Direct measurement of cavity gauge pressure as a function of the clapping speed showing a nearly quadratic scaling, matching with Eq. (11). The dashed line fits the scattered data onto $[P_{cavity}]_{max} = a\,u_{clap}^2$, resulting in an adjusted R-square of 0.72. The dotted line fits the scattered data onto $[P_{cavity}]_{max} = a\,u_{clap}^b$, resulting in a power of $b \approx 1.6$ and an adjusted R-square of 0.74.

Newton's second law, $F = m\frac{du}{dt} \approx m\,u_{clap}/\delta t$, and Hooke's law, $\delta N = (NP_{cavity})/E$, we can express

$$\delta H = \frac{1}{E}\left(\frac{m(N+H)u_{clap}}{A\delta t} - NP_{cavity}\right). \tag{9}$$

Substituting δt by l/u_{clap} where l is a characteristic length for collision, we plug Eq. (9) into Eq. (7) and get

$$\delta V = \frac{\pi(R^2+H^2)}{E}\left(\frac{m(H+N)u_{clap}^2}{lA} - NP_{cavity}\right). \tag{10}$$

Following the adiabatic relation, $P_{cavity} = \gamma P_{atm}\delta V/V$, we can finally draw the relationship between P_{cavity} and u_{clap} as

$$P_{cavity} = \frac{Km(H+N)}{lA(1+NK)}u_{clap}^2, \tag{11a}$$

$$K = \frac{\gamma\pi P_{atm}(R^2+H^2)}{VE}. \tag{11b}$$

This scaling predicts a quadratic relationship between P_{cavity} and u_{clap}, which was confirmed by the experimental results in Fig. 8(c), regardless of configuration or material. One may notice that P_{cavity} are generally around two orders of magnitude higher than the initial sound pressure (compare Figs. 8(b) and 8(c)]. This suggests that most of the energy contributes to the expulsion of the strong air jet while only a small portion is used to create the acoustic wave disturbance.

E. Temporal decay of the sound

Perceptually, people do not typically hear the characteristic long-lasting sound from resonating HR chambers in hand claps. This phenomenon is explained by the rate of energy attenuation in air molecule oscillations, which is typically characterized by the quality factor Q. Q represents the ratio of the total energy stored to the energy dissipated in each oscillation cycle, such that a lower Q corresponds to a faster energy attenuation [Fig. 9(a)]. Intuitively, it indicates how quickly a sound signal attenuates from an audible to an inaudible level. In an ideal clapping sound, the signal is a damped simple harmonic oscillation, and mathematically, Q is an inverse of the exponential decay rate of the sound signal τ as $Q = 2\pi f\tau^{-1}$. In the frequency domain, Q is commonly defined as the ratio of the resonance frequency to the bandwidth at 50% power (see dashed lines in Fig. 5(a) and Supplemental Material Sec. I E [37]) and expressed as

$$Q = \frac{f_{resonance}}{\Delta f_{50\%\ power}}. \tag{12}$$

Overall, the configuration changes had limited impact on Q [Fig. 9(b)]. Two observations can be made here: (1) for the same configuration, faster u_{clap} results in lower Q, and (2) Q tends to slightly increase with a bigger S. Motion tracking [45] of the outlet flanges [Fig. 9(c)] demonstrated the importance of transient outlet deformation to Q. A higher clapping speed potentially experiences more outlet squeezing [Fig. 9(ci)], a larger initial rebound [Fig. 9(cii)], and persisting trailing oscillation [Fig. 9(ciii) and 9(civ)], constantly sweeping S in a relatively larger range during the sound-producing period. This geometry fluctuation (Supplemental Movie S3 [37]) causes the hand HR to resonate at slightly different natural frequencies at each time instant as the jet expels outside the cavity, resulting in a broader-band resonance peak and hence a lower Q. As in Fig. 9(d), Q and max outlet deformation ($[\Delta(h/h_{t=\infty})]_{max}$) experience opposite trends with increasing u_{clap}. As for the slight Q shift across S1–S5, the physical model's design strategy was to increase the arch curvature height h while keeping the neck width w constant to increase the outlet area S. This enabled the bigger (rounder) outlet to withstand more stress than the smaller (slenderer) outlet, less prone to deformation (Supplemental Movie S3 [37]), and hence a relatively narrower frequency band and a higher Q. From the energy loss perspective, more outlet deformation would increase the losses through viscoelastic damping, structural damping, and boundary layer viscous dissipation, resulting in a faster sound level decay.

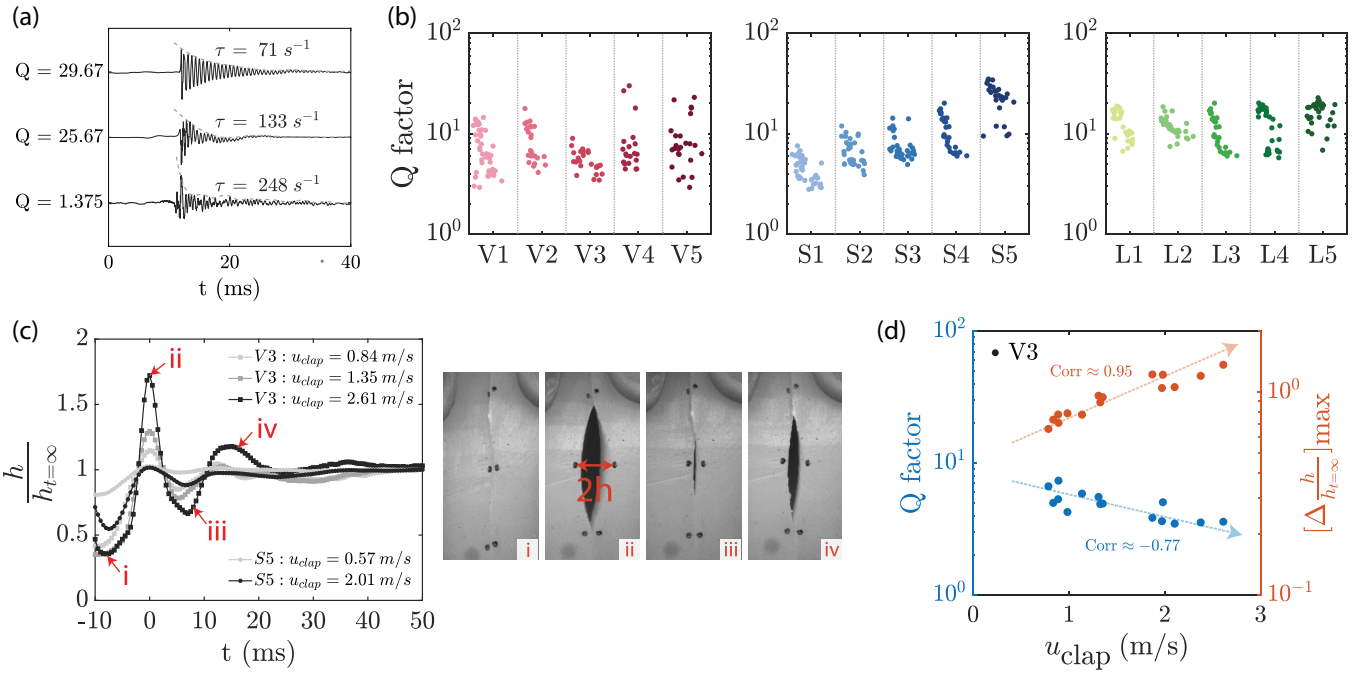

FIG. 9. Determinants of temporal dissipation of the clapping sound. (a) Illustration of the physical meaning of Q. The top two signals are from clapping replicas and the third signal is from clapping human hands. Dashed curves represent the envelopes of the damping signals by the exponential decay function of $P = P_0 e^{-\tau t}$, where τ is the temporal exponential decay rate. (b) Experimental results of Q from Ecoflex 0030 replicas of different geometries. Each scatter point represents one clap signal. Separated by dotted lines, each vertical section has a linear scale for $u_{\text{clap}} \in [0, 4]$ m/s from left to right. (c) Postcollision oscillatory outlet deformation from silicone replica claps of different u_{clap} and S. The plot denotes the distance between the center tracer markers over time, normalized by the same distance after all deformations damp out (Tracking software: DLTdv8 [45]). Photos on the right help visualize the deformation at four critical timestamps. Note: The time axis here aligns the peak deformation to $t = 0$ ms to facilitate comparison. This time axis should not be confused with those in Figs. 4 and 5 since it does not reflect synchronization. (d) Opposite trends of Q and maximum outlet deformation as a function of u_{clap}. $[\Delta(h/h_{t=\infty})]_{\max}$ refers to the maximum outlet deformation, calculated as the difference between the maximum and minimum values on the same curve in (c).

Compared with the classical HR model, our clapping results also showed much lower Q than the theoretical lossless resonators. For a rigid-wall statically excited HR with no energy losses but acoustic radiation, Q is calculated as $Q = 4\pi\sqrt{V(L'/S)^3}$ [21], which, for our dimensions in Table I, falls in the range of 74–448. The uniformly low Q for clapping sounds indicated a more rapid energy decay and a shorter duration resulting from the elastic deformation of the outlet than in resonating rigid and loss-less HR chambers. This discrepancy between clapping sounds and the ideal classical HR provides a physical understanding of the short-lasting real-life perception.

IV. DISCUSSION AND CONCLUSION

In this study, we presented a thorough investigation into the physical process of hand-clapping sound production. We confirmed the hypothesis that hand clapping is a flow-excited HR rather than merely a solid collision sound. Parametric experiments and numerical simulations demonstrated that the frequency of clapping sound could be accurately predicted by a classical HR theory for both engineered and authentic human hands. Our results validated the frequency dependence on hand configuration, namely three fundamental hand geometries V, S, and L', through which reduced-order modeling became accessible. We showed that the material elasticity and the transient collision deformation have minor effects on frequency yet nontrivial effects on other sound properties including initial intensities and energy dissipation. The shape and size fluctuations at the neck outlet after collision lead to the faster attenuation of clapping sound signals than that from a statically excited rigid-wall HR. Other factors for this faster energy loss may also include the viscous boundary layer around the impulsive jet flow [46] and the elastic energy-absorbing lining material [43], but further work involving 3D topology tracking of the interior and static excitation experiments on elastic-wall resonators is necessary to quantify their contributions. These results motivate us to incorporate more sex- and age-related skin tissue property variations [47–50] in future studies with human participants to evaluate potential individual traits in hand clapping sounds. Moreover, our collision mechanics model provided a better understanding of the palm cavity gauge pressure as a function of the clapping speed, potentially directing us closer to decoding the factors for the initial sound intensity of hand claps. Last, we briefly examined the spatial propagation of the handclapping sound in distances far beyond one wavelength. (Relevant experimental and simulation methods in Appendix E.) Once the sound is emitted from the generation site, the source can be seen as a point and the signal can be modeled as a spherically propagating wavefront. Mathematically, P is inversely proportional to the distance r. Results from the replicas, humans, and

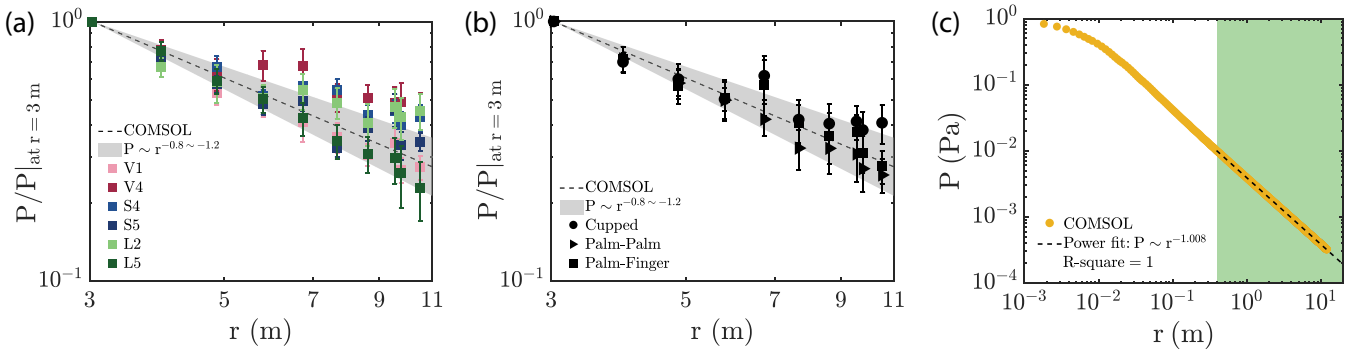

FIG. 10. Handclapping sound spatial propagation far from the source, obtained from (a) silicone replicas, (b) humans, and (c) simulations.

simulations showed that all cases consistently followed the inverse proportionality, as expected (Fig. 10). It is worth noting that, given the attenuation coefficient of sound energy absorption in air [51], the frequency dependence of attenuation in hand clapping is likely too small to be detected [Figs. 10(a) and 10(b)], and any relevant effects are probably negligible for practical applications of hand clapping for communication. Our work provided the first experimental support for the theoretical framework and improved the fundamental understanding of hand claps for broader application potentials.

ACKNOWLEDGMENTS

We thank Ramit A. Machhan for his participation in the theoretical modeling and measurements of cavity gauge pressure. The research is partially supported by the National Science Foundation (NSF CBET-2401507). Experiments involving human participants adhere to the Institutional Review Board ethical approval protocol (IRB 0146509). All human data acquisition was guaranteed to have no personal identification information including names, fingerprints, and faces documented. All participants voluntarily gave consent to the usage and publication of their data in an academic format.

S.J. conceived the idea; Y.F., A.K., G.L., L.Z., and S.J. designed the research; Y.F., A.K., G.L., L.Z., and S.J. performed the research; Y.F., A.K., and G.L. analyzed the data; Y.F. wrote the paper; and Y.F., A.K., G.L., L.Z., and S.J. reviewed the paper.

The authors declare no competing interests.

DATA AVAILABILITY

Data generated and analyzed during the study is available on the Open Science Framework (DOI 10.17605/OSF.IO/CQT7D). Source data containing human participants are available on reasonable request to Y.F. and S.J.

APPENDIX A: SOFT MATERIAL PROPERTY CHARACTERIZATION

1. Instron compression test

An Instron machine with compression test modules [Fig. 11(a)] was used to measure the elastic moduli of soft materials under relatively slow (with respect to handclap collisions) loading conditions. Each soft polymer was cast into a circular cylinder of a known cross-sectional area. Axial

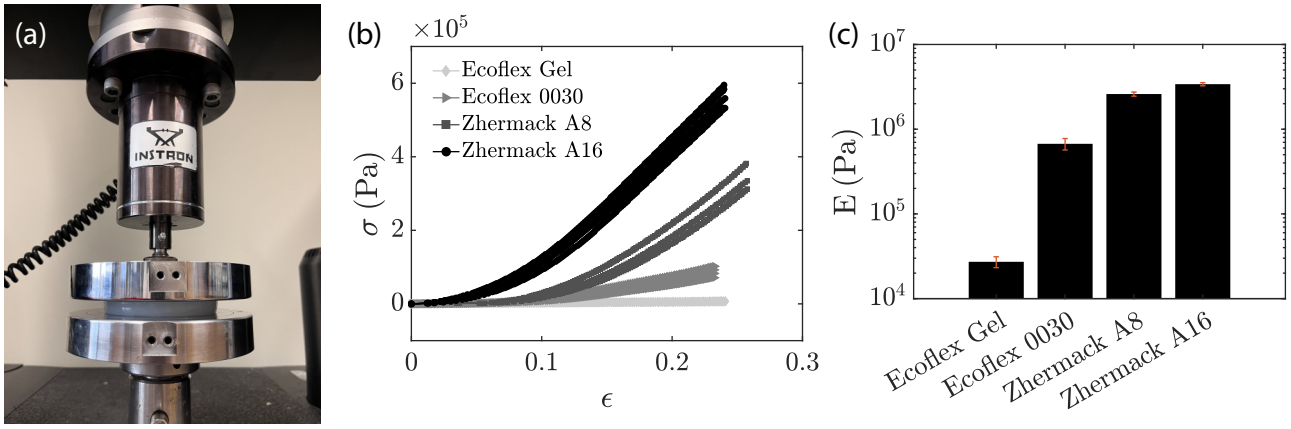

FIG. 11. Measurement of the elastic modulus (E) by compression test. (a) A picture of the Instron compression test on the Ecoflex 0030 sample. (b) Stress-strain curves of four elastomer samples, each repeated for five trials. (c) Order-of-magnitude comparison of the elastic moduli of four elastomer samples. Error bars represent standard deviations. The trend of the measured E matches with the trend of the shore hardness values reported by the manufacturers. Durometer Shore hardness from the manufacturers for Ecoflex Gel is 000-35, for Ecoflex 0030 is 00-30, for Zhermack A8 is A-8, and for Zhermack A16 is A-16.

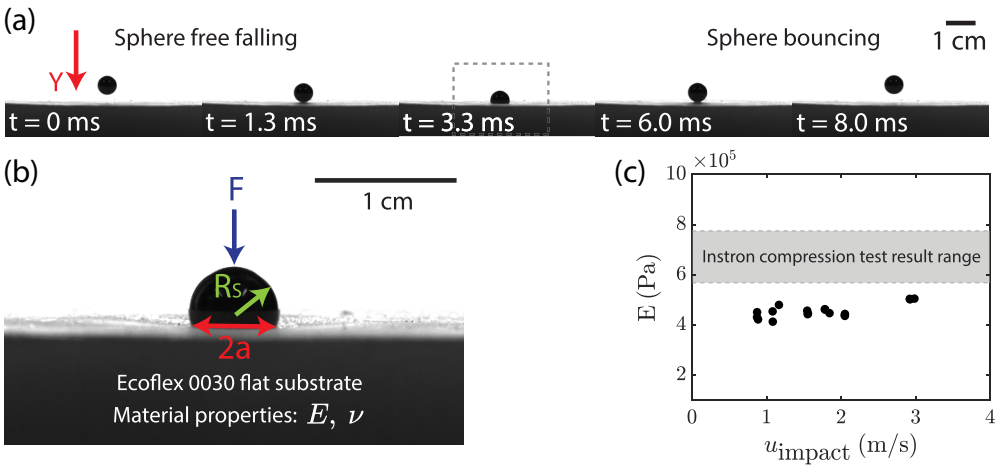

FIG. 12. Measurements of the elastic modulus (E) under different impact speeds by Hertz contact theory. (a) Time series of a small stainless steel sphere dropping and impacting a flat Ecoflex 0030 substrate in the Hertz ball drop test. (b) Snapshot of the largest deformation due to impact with important quantities labeled. (c) Near-constant elastic moduli from the Hertz contact theory compared with the aforementioned Instron compression test results.

compression loading was applied at 1000 mm/min speed until deformation reached 3 mm. Near-linear portions of the stress-strain curves ($\epsilon > 0.18$) were fit to the function of $\sigma = E\,\epsilon$ [Figs. 11(b) and 11(c)].

2. Hertz Ball drop test

To verify the negligible material viscoelasticity within our range of experiments, Hertz ball drop tests were conducted to measure the elastic moduli under relatively fast (with respect to handclap collision) loading conditions. A stainless steel sphere (radius = 3.175 mm) was dropped vertically from different heights in a free fall to impact a flat Ecoflex 0030 substrate (radius = 45 mm) [Fig. 12(a)]. The initial impact was recorded horizontally by a high-speed camera (Photron Fastcam NOVA S6) at 10 000 fps. The apex point of the sphere was tracked using DLTdv8 [45], from which velocity and acceleration of the sphere were calculated using the same method in Appendix D. At maximum substrate deformation, the sphere's velocity became zero and the substrate experienced a contact force F. The largest deformation is associated with a contact radius of a, which is measurable from the footage [Fig. 12(b)]. Hertz contact theory can be readily found in the literature [52] as

$$a^3 = \frac{3FR_s}{4E'}, \tag{A1}$$

where E' is the effective elastic modulus of the system. Specifically, $\frac{1}{E'} = [\frac{1-\nu^2}{E}]_{\text{Ecoflex 0030}} + [\frac{1-\nu^2}{E}]_{\text{Stainless steel}}$, where E is the Young's modulus and ν is the Poisson's ratio. Since stainless steel is much stiffer than Ecoflex 0030, we take the first-order approximation that $E' = [\frac{E}{1-\nu^2}]_{\text{Ecoflex 0030}}$ and $\nu \approx 0.45$. Results show that despite the viscoelasticity of the silicone material [53], within the impact speed range for handclaps (0–4 m/s), the elastic modulus remains constant, acting like a linear-elastic (Hookean) material. The Hertz ball drop yielded E values slightly lower than the Instron compression test but well within the same order of magnitude [Fig. 12(c)]. This difference is thought to be attributed to uncertainties in the measurement of the contact radius a or the strain ϵ.

APPENDIX B: SIMULATION MESH VALIDATION

To check the numerical convergence, a series of simulations for configuration S4 with varying mesh element sizes under the settings described in Sec. II C were conducted. The maximum element size was varied by three levels, 3.09, 6.18, and 12.36 mm, corresponding to 0.05λ, 0.1λ, and 0.2λ, respectively. As shown in Fig. 13, great consistency was observed among all mesh sizes, confirming that the selected standard mesh size, $\delta_{\max} = 0.1\lambda_{\min} = 6.18$ mm, was suitable and adequate. Specifically, the resonance frequencies for all three mesh sizes were the same, 703.702 Hz. The frequency scan step at this frequency was 15.226 Hz. That means, doubling or halving the spatial resolution led to no changes in the computed resonance frequency with a percentage uncertainty of 15.226 Hz/703.702 Hz = 2.1637%.

APPENDIX C: THE SPRING-MASS SYSTEM OF THE HR [21]

Traditional HRs consist of a large cavity and a small necked outlet for air to move in and outward. When resonating, a longitudinal wave of air molecules along the neck would

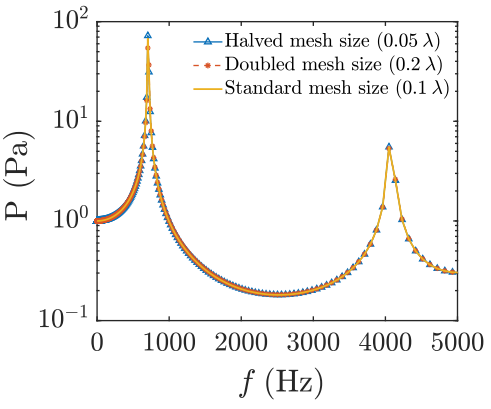

FIG. 13. Numerical convergence among variable mesh sizes.

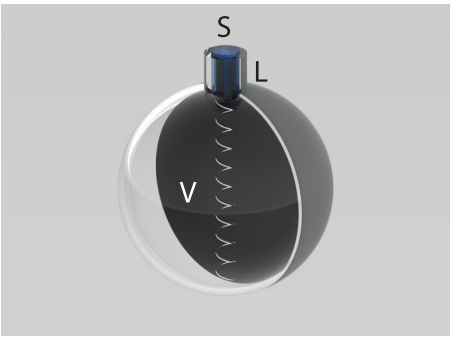

FIG. 14. Three-dimensional render illustration of the spring-mass system analogy of HRs.

propagate the disturbance into the surrounding space. This longitudinal compression and rarefaction of the air molecules within the neck can be viewed as an air column oscillating altogether, being pushed and pulled by a spring. This analogy simplifies the HR resonance to a well-understood spring-mass system (Fig. 14).

The air column in the neck of the HR has a cross-sectional area of S, a length of L, a density of ρ, a mass of m, and a specific heat ratio of γ. In sound production, the air column is perturbed by a change of pressure δP and oscillates along the neck by a displacement x from the equilibrium position. We can express the equation of motion for the air column as

$$\frac{d^2x}{dt^2} = \frac{F}{m} = \frac{\delta P}{\rho L}. \tag{C1}$$

Applying the adiabatic relations to the air in the HR cavity, we can express δP as a function of the finite change in cavity volume δV as

$$\delta P = -\frac{\gamma P_{\text{atm}} \delta V}{V}, \tag{C2}$$

where P_{atm} is the ambient air pressure and δV can be further expressed as $\delta V = Sx$. Plugging Eq. (C2) into Eq. (C1) will result in

$$\frac{d^2x}{dt^2} = -\frac{\gamma P_{\text{atm}} S}{\rho L V} x. \tag{C3}$$

Following a simple harmonic oscillation of the spring-mass system which has a resonance frequency of $f = (1/2\pi)\sqrt{k/m}$, where k is the spring constant, the resonance frequency of the HR can be expressed as

$$f = \frac{c}{2\pi}\sqrt{\frac{S}{VL'}}, \tag{C4}$$

where $c = \sqrt{\gamma P_{\text{atm}}/\rho}$ is the speed of sound in air, taken as 340 m/s in our study. In Eq. (C4), L' is used to incorporate a common neck length correction on L due to the radiative effect of the air column motion. For the geometries in our study, the hand clapping HR would be considered unflanged on both ends of the neck, resulting in $L' = L + 1.2\sqrt{S/\pi}$.

APPENDIX D: MECHANICAL DROP TEST

To verify negligible human factors within regular hand-held tests, 6 representative mechanical drop tests were performed for comparison. During mechanical drop tests on silicone replicas, the bottom receiving piece was laid flat on a metal optics table and the top piece was hung above by a thin fishing line at a certain height. On confirming a decent alignment, the top piece was released into a free fall to clap with the bottom piece [Fig. 15(a)]. Four black tracers were

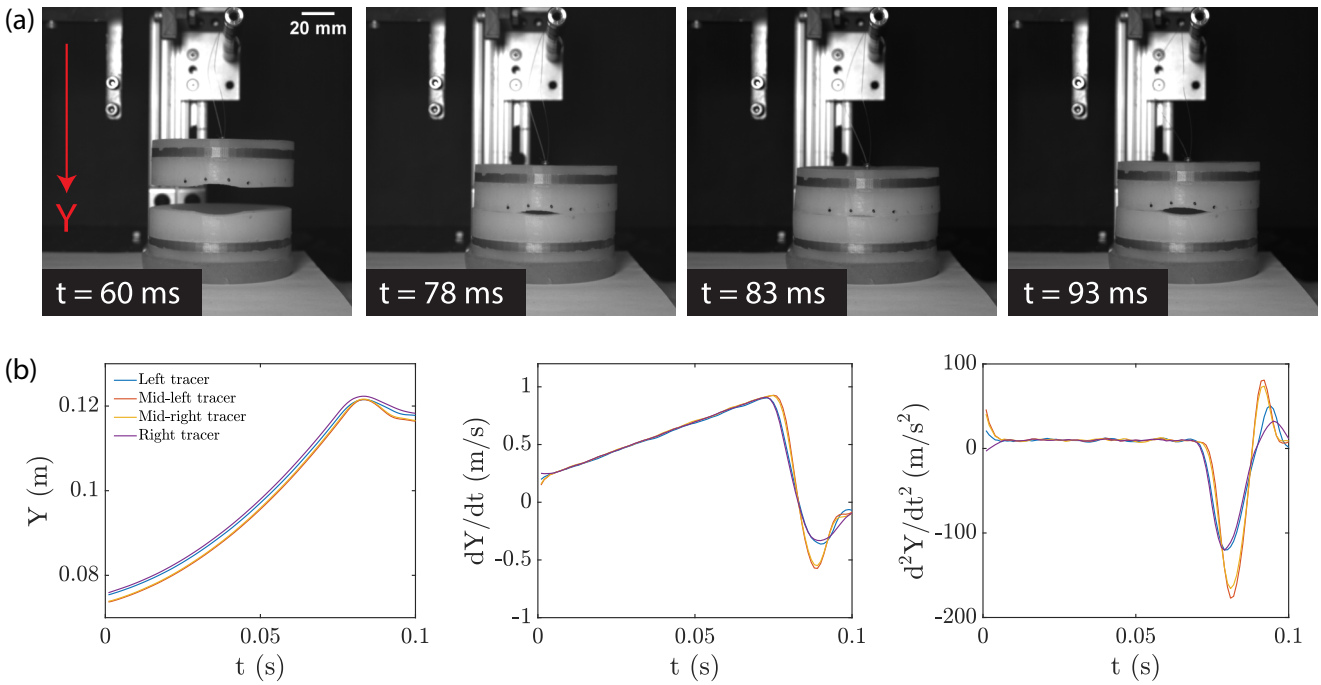

FIG. 15. Mechanical drop test validation. (a) Time series of the mechanical drop test example with V3 Ecoflex 0030 replicas. (b) Motion tracking results from DLTdv8 [45].

put around the outlet for motion tracking, from which impact velocity and acceleration can be calculated. Vertically downward following gravity was defined as the positive Y direction. Good consistency between the side tracers and the middle tracers was seen. Impact velocity (u_{clap}) was recorded as the maximum value of the velocity [Fig. 15(b)]. Note that for acceleration, the middle two tracers had larger magnitudes than the side two tracers because of the uneven curvature at the outlet and material rebound. Mechanical dropping was theoretically unaffected by human factors and more repeatable, but in reality, was flawed, since a good alignment was hard to achieve and the table/support introduced unnecessary structural noises. We determined the hand-held tests were more repeatable and reliable due to human's familiarity with the clapping limb motion and the fabulous structural damping of the muscles and joints. Therefore, all replica data in this work were acquired in the hand-held test method unless marked as "mechanical drop."

APPENDIX E: SPATIAL PROPAGATION OF THE HANDCLAPPING SOUND

1. Measurements far from the sound source

Handclaps were administered in an auditorium where temperature, humidity, and ambient pressure were maintained similarly to the experimental setting in Sec. II B [Fig. 16(a)]. One person stood at a designated location in the front of the room and clapped consecutively around 20 times for each replica pair or hand configuration. Ten stand-alone microphones (Sunlan) were positioned at various distances from the clap source, covering about 6–20 wavelengths of the signal (i.e., 3–11 m). The wavelengths of all cases were predicted to be roughly 0.2–0.8 m. The microphones were oriented toward the sound source with no structural obstruction. Each clap was recorded simultaneously by all microphones, for which the quality was set to 1536 kbps in WAV format with -1 to $+1$ cutoff boundaries so that full-scale decibel (dB-FS) values could be computed. A sound level meter (QUEST model 2400) was used to measure the background sound pressure level in dB-SPL so that clap signal units could be converted from dB-FS to dB-SPL and Pascal to have real physical meanings. A multimodal calibration across the 10 microphones was conducted using a waveform generator (SIGLENT SDG 2042 X; MonKey MAMP4 Digital Bluetooth Amplifier; gain set to 0 dB.) in the same room. Continuous sound signals at various frequencies in the range of 300–3000 Hz were generated and simultaneously recorded on all ten microphones from 3 m away. The sound level in the first microphone was used as a baseline. Differences between the sound levels in the other microphones and the first baseline were treated as correction coefficients to calibrate all devices.

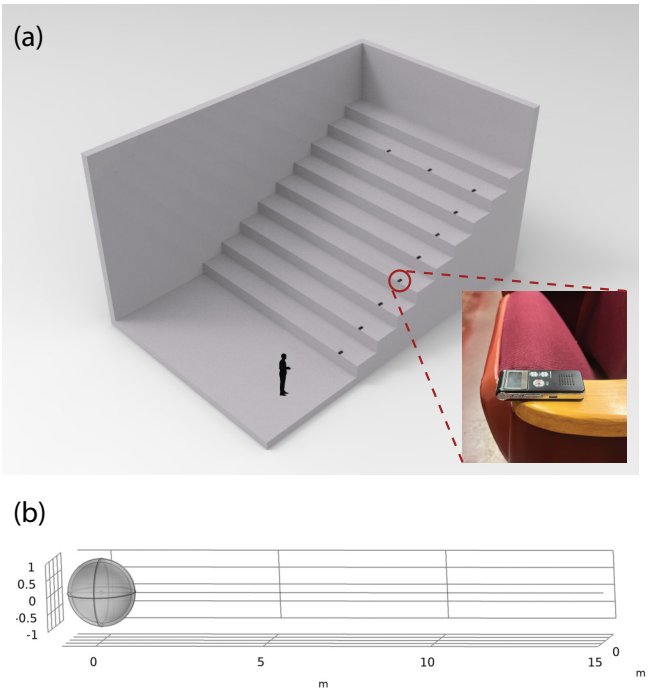

FIG. 16. Methods for investigating sound spatial propagation. (a) Experimental setup in an auditorium. Black objects are microphones, with a real image shown as the inset. The relative position arrangement of the ten microphones is realistic, but the schematic dimension is not scaled to reality. (b) Simulation setup for the far-field. The sphere is the PML layer mentioned in Sec. II C, within which near-field results were obtained.

2. Simulations far from the sound source

COMSOL Multiphysics simulations were constructed for 1–15 m from the sound source [Fig. 16(b)]. To reduce the computational cost, we employed the "exterior field calculation" method to compute the pressure field beyond the simulated domain of the 1 m radius sphere. The exterior field calculation approach, based on the Helmholtz-Kirchhoff integral representation, computes the pressure outside the simulated domain as a boundary integral, utilizing quantities evaluated on the surface.

[1] Z. Néda, E. Ravasz, Y. Brechet, T. Vicsek, and A.-L. Barabási, The sound of many hands clapping, Nature (London) **403**, 849 (2000).
[2] P. Tranchant, D. T. Vuvan, and I. Peretz, Keeping the beat: A large sample study of bouncing and clapping to music, PLoS ONE **11**, e0160178 (2016).
[3] K. E. Batchelor and W. P. Bintz, Hand-clap songs across the curriculum, Reading Teach. **65**, 341 (2012).
[4] E. Harwood, Music learning in context: A playground tale, Res. Stud. Music Educ. **11**, 52 (1998).
[5] A. P. Merriam, Characteristics of African music*, J. Int. Folk Music Council **11**, 13 (1959).
[6] Y. Zhang, F. Baills, and P. Prieto, Hand-clapping to the rhythm of newly learned words improves l2 pronunciation: Evidence from training chinese adolescents with french words, Lang. Teach. Res. **24**, 666 (2020).
[7] F. Baills and P. Prieto, Embodying rhythmic properties of a foreign language through hand-clapping helps children to better pronounce words, Lang. Teach. Re. **27**, 6 (2021).

[8] P. Seetharaman and S. P. Tarzia, The hand clap as an impulse source for measuring room acoustics, in *Audio Engineering Society Convention 132* (Audio Engineering Society, New York, 2012).

[9] N. M. Papadakis and G. E. Stavroulakis, Handclap for acoustic measurements: Optimal application and limitations, in *Acoustics* (MDPI, Basel, 2020), Vol. 2, pp. 224–245.

[10] R. de Vos, N. M. Papadakis, and G. E. Stavroulakis, Improved source characteristics of a handclap for acoustic measurements: Utilization of a leather glove, in *Acoustics* (MDPI, Basel, 2020), Vol. 2, pp. 803–811.

[11] M. S. Rasel, P. Maharjan, and J. Y. Park, Hand clapping inspired integrated multilayer hybrid nanogenerator as a wearable and universal power source for portable electronics, Nano Energy **63**, 103816 (2019).

[12] M. J. Kim, J. H. Hong, and S. H. Jang, The cortical effect of clapping in the human brain: A functional MRI study, NeuroRehabilitation **28**, 75 (2011).

[13] A. Jylhä and C. Erkut, A hand clap interface for sonic interaction with the computer, in *CHI'09 Extended Abstracts on Human Factors in Computing Systems* (ACM, New York, 2009), pp. 3175–3180.

[14] C. Wróbel and S. K. Zieliński, Identification of humans using hand clapping sounds, in *Proceedings of the Computer Information Systems and Industrial Management: 20th International Conference (CISIM 2021)* (Springer, Berlin, 2021), pp. 66–77.

[15] H. Meng, N. Pears, and C. Bailey, A human action recognition system for embedded computer vision application, in *Proceedings of the IEEE Conference on Computer Vision and Pattern Recognition* (IEEE, Los Alamitos, CA, 2007), pp. 1–6.

[16] S. Gart, B. Chang, B. Slama, R. Goodnight, S. H. Um, and S. Jung, Dynamics of squeezing fluids: Clapping wet hands, Phys. Rev. E **88**, 023007 (2013).

[17] R. Acharya, E. J. Challita, M. Ilton, and M. S. Bhamla, The ultrafast snap of a finger is mediated by skin friction, J. R. Soc. Interface. **18**, 20210672 (2021).

[18] B. H. Repp, The sound of two hands clapping: An exploratory study, J. Acoust. Soc. Am. **81**, 1100 (1987).

[19] N. H. Fletcher, Shock waves and the sound of a hand-clap–A simple model, Acoust. Aust **41**, 165 (2013).

[20] M. J. Hargather, G. S. Settles, and M. J. Madalis, Schlieren imaging of loud sounds and weak shock waves in air near the limit of visibility, Shock Waves **20**, 9 (2010).

[21] L. E. Kinsler, A. R. Frey, A. B. Coppens, and J. V. Sanders, *Fundamentals of Acoustics* (John Wiley & Sons, New York, 2000).

[22] W. K. Blake, *Mechanics of Flow-induced Sound and Vibration, Volume 2: Complex Flow–Structure Interactions* (Academic Press, San Diego, CA, 2017).

[23] F. Kraxberger, A. Wurzinger, and S. Schoder, Machine-learning applied to classify flow-induced sound parameters from simulated human voice, arXiv:2207.09265.

[24] G. Gillot, C. Derec, J.-M. Genevaux, L. Simon, and L. Benyahia, A new insight on a mechanism of airborne and underwater sound of a drop impacting a liquid surface, Phys. Fluids **32**, 062004 (2020).

[25] M. Boudina, J. Kim, and H.-Y. Kim, Amplitude of water pouring sound, Phys. Rev. Fluids **8**, L122002 (2023).

[26] R. Ma, P. E. Slaboch, and S. C. Morris, Fluid mechanics of the flow-excited Helmholtz resonator, J. Fluid Mech. **623**, 1 (2009).

[27] F. Ghanadi, M. Arjomandi, B. Cazzolato, and A. Zander, Interaction of a flow-excited helmholtz resonator with a grazing turbulent boundary layer, Exp. Therm Fluid Sci. **58**, 80 (2014).

[28] P. K. Tang and W. A. Sirignano, Theory of a generalized Helmholtz resonator, J. Sound Vib. **26**, 247 (1973).

[29] R. C. Chanaud, Effects of geometry on the resonance frequency of Helmholtz resonators, J. Sound Vib. **178**, 337 (1994).

[30] A. Selamet and I. Lee, Helmholtz resonator with extended neck, J. Acoust. Soc. Am. **113**, 1975 (2003).

[31] X. Wang and C.-M. Mak, Wave propagation in a duct with a periodic Helmholtz resonators array, J. Acoust. Soc. Am. **131**, 1172 (2012).

[32] C. Cai and C. M. Mak, Acoustic performance of different Helmholtz resonator array configurations, Appl. Acoust. **130**, 204 (2018).

[33] V. Gibiat, An acoustic study of ceramic traditional whistles, in *Proceedings of Meetings on Acoustics* (AIP, Melville, NY, 2013), Vol. 19.

[34] V. L. Jordan, The application of helmholtz resonators to sound-absorbing structures, J. Acoust. Soc. Am. **19**, 972 (1947).

[35] T. Jonsson, B. D. Chivers, K. R. Brown, F. A. Sarria-S, M. Walker, and F. Montealegre-Z, Chamber music: an unusual Helmholtz resonator for song amplification in a neotropical bush-cricket (orthoptera, tettigoniidae), J. Exp. Biol. **220**, 2900 (2017).

[36] L. Peltola, C. Erkut, P. R. Cook, and V. Valimaki, Synthesis of hand clapping sounds, IEEE Trans. Aud. Speech Lang. Process. **15**, 1021 (2007).

[37] See Supplemental Material at http://link.aps.org/supplemental/10.1103/PhysRevResearch.7.013259 for supplemental results, auxiliary validations, raw human data, and descriptions of the supplemental movies.

[38] X. Liang and S. A. Boppart, Biomechanical properties of *in vivo* human skin from dynamic optical coherence elastography, IEEE Trans. Biomed. Eng. **57**, 953 (2009).

[39] A. Kalra, A. Lowe, and A. M. Al-Jumaily, Mechanical behaviour of skin: A review, J. Mater. Sci. Eng. **5**, 1000254 (2016).

[40] P. Boonvisut and M. C. Çavuşoğlu, Estimation of soft tissue mechanical parameters from robotic manipulation data, IEEE/ASME Trans. Mechatr. **18**, 1602 (2012).

[41] Y.-L. Park, C. Majidi, R. Kramer, P. Bérard, and R. J. Wood, Hyperelastic pressure sensing with a liquid-embedded elastomer, J. Micromech. Microeng. **20**, 125029 (2010).

[42] D. M. Photiadis, The effect of wall elasticity on the properties of a Helmholtz resonator, J. Acoust. Soc. Am. **90**, 1188 (1991).

[43] A. Selamet, M. B. Xu, I.-J. Lee, and N. T. Huff, Helmholtz resonator lined with absorbing material, J. Acoust. Soc. Am. **117**, 725 (2005).

[44] Y. Chen and Y.-H. Park, A Helmholtz resonator on elastic foundation for measurement of the elastic coefficient of human skin, J. Mech. Behav. Biomed. Mater. **101**, 103417 (2020).

[45] T. L. Hedrick, Software techniques for two-and three-dimensional kinematic measurements of biological and biomimetic systems, Bioinspir. Biomimet. **3**, 034001 (2008).

[46] Y. A. Ilinskii, B. Lipkens, and E. A. Zabolotskaya, Energy losses in an acoustical resonator, J. Acoust. Soc. Am. **109**, 1859 (2001).

[47] H. S. Ryu, Y. H. Joo, S. O. Kim, K. C. Park, and S. W. Youn, Influence of age and regional differences on skin elasticity as measured by the cutometer, Skin Res. Technol. **14**, 354 (2008).

[48] E. Carmeli, H. Patish, and R. Coleman, The aging hand, J. Gerontol. Ser. A: Biol. Sci. Med. Sci. **58**, M146 (2003).

[49] P. G. Agache, C. Monneur, J. L. Leveque, and J. De Rigal, Mechanical properties and Young's modulus of human skin in vivo, Arch. Dermatol. Res. **269**, 221 (1980).

[50] D. L. Bader and P. Bowker, Mechanical characteristics of skin and underlying tissues in vivo, Biomaterials **4**, 305 (1983).

[51] H. E. Bass, L. C. Sutherland, A. J. Zuckerwar, D. T. Blackstock, and D. M. Hester, Atmospheric absorption of sound: Further developments, J. Acoust. Soc. Am. **97**, 680 (1995).

[52] A. C. Fischer-Cripps, The Hertzian contact surface, J. Mater. Sci. **34**, 129 (1999).

[53] Z. Liao, M. Hossain, X. Yao, R. Navaratne, and G. Chagnon, A comprehensive thermo-viscoelastic experimental investigation of ecoflex polymer, Polymer Testing **86**, 106478 (2020).